

# Total-Body Quantitative Parametric Imaging of Early Kinetics of FDG

**Running title:** Fast total-body PET parametric imaging

**Authors:** Tao Feng<sup>1</sup>, Yizhang Zhao<sup>2</sup>, Hongcheng Shi<sup>3</sup>, Hongdi Li<sup>1</sup>, Xuezhu Zhang<sup>4</sup>, Guobao Wang<sup>4</sup>, Patricia M. Price<sup>5</sup>, Ramsey D. Badawi<sup>4,6</sup>, Simon R. Cherry<sup>4,6</sup> and Terry Jones<sup>6</sup>

**Affiliations:** <sup>1</sup>UIH America Inc. TX, USA

<sup>2</sup>United Imaging Healthcare, Shanghai, China;

<sup>3</sup>Zhongshan Hospital, Fudan University, Shanghai, China

<sup>4</sup>Department of Biomedical Engineering, University of California, Davis, CA, USA;

<sup>5</sup>Imperial College London, London, United Kingdom

<sup>6</sup>Department of Radiology, University of California Davis Medical Center, CA, USA;

**First author:** Tao Feng, UIH America, Inc. 9230 Kirby Dr, Suite 600, Houston, TX, 77054 USA E-mail: [tao.feng@united-imaging.com](mailto:tao.feng@united-imaging.com), Phone: +1(443)927-6712, Fax: (281)709-6856

**Corresponding author:** The same

**Word count:** 5000

**Figures:** 6

**Tables:** 1

**Financial support:** This work was partially supported by the National Institutes of Health under Grant R01 CA206187.

## ABSTRACT

Parametric imaging has been shown to provide better quantitation physiologically compared with SUV imaging in PET. With the increased sensitivity from a recently developed total-body PET scanner, whole-body scans with higher temporal resolution become possible for dynamic analysis and parametric imaging. In this paper, we focus on deriving the parameter  $k_1$  using compartmental modeling, and on developing a method to acquire whole-body FDG-PET parametric images using only the first 90 seconds of the post-injection scan data with the total-body PET system.

Dynamic projections were acquired with a time interval of 1 second for the first 30 seconds and 2 seconds for the following minute. Image-derived input functions were acquired from the reconstructed dynamic sequences in the ascending aorta. The one-tissue compartment model with the total of 4 parameters ( $k_1$ ,  $k_2$ , blood fraction, delay time) was used. A maximum-likelihood based estimation method was developed with the 1-tissue compartment model solution. The accuracy of the acquired parameters was compared with the ones estimated using a 2-tissue irreversible model with 1-hour long data.

All four parametric images were successfully calculated using data from two volunteers. By comparing the time-activity-curves acquired from the volume of interests, it was shown that the parameters estimated using our method were able to predict the time-activity curves of the early dynamics of FDG in different organs. The time delay effects for different organs were also clearly visible in the reconstructed time delay image with delay variations as large as 40 seconds. The estimated parameters using both 90 seconds data and 1-hour long data were in good agreement for  $k_1$  and blood fraction, while a large difference of  $k_2$  was found between the 90 seconds and 1-hour data, suggesting  $k_2$  can't be reliably estimated from the 90 second scan.

We have shown that with the use of total-body PET and the increased sensitivity, it is possible to estimate parametric images based on the very early dynamics following FDG injection. The estimated  $k_1$  could potentially be used clinically as an indicator for identifying abnormalities.

*Key words— Parametric imaging, early dynamic, total-body PET, compartment model*

## INTRODUCTION

Conventional PET imaging makes widespread use of standard uptake values (SUV) for semi-quantitative analysis, especially in measurements of  $^{18}\text{F}$ -fluorodeoxyglucose (FDG) uptake in tumors (1). However, SUV depends on the time of measurement and many other factors (2,3), which makes reliable quantitation a challenging task. On the other hand, kinetic analysis in PET has more direct physiological meaning than the SUV, and can be a more robust approach for quantifying FDG uptake and utilization (4,5).

Compared with the volume-of-interest (VOI) based kinetic analysis (6,7), parametric imaging enables the acquisition of voxel-level dynamics of the tracer uptake by applying kinetic modeling for each individual voxel (8,9). Conventional graphical methods including Logan analysis (10) and Patlak analysis (11) have been utilized for parametric imaging because of their linear properties and simplicity in acquisition protocols. Improved lesion contrast and detectability have been demonstrated by many studies (12,13). With the assumption that the dynamic activity can be described using exponentials as impulse responses, the basis function approach provides a possible approach for non-linear model fitting (14,15). Recently, whole-body parametric imaging using the Patlak model has been proposed using a multi-pass acquisition protocol (16,17).

Even with the many added benefits of kinetic modeling, parametric imaging techniques and dynamic protocols are not widely used in clinical studies, especially in oncology (17). In some studies, the requirement of invasive arterial blood sampling for the input function makes the scan protocol impractical. Even with the use of image-derived input functions (18,19) or population-based input functions (20,21), a minimal scan time of 30 minutes is often required to reveal dynamic information using Patlak analysis. Compared with state-of-art whole-body SUV scans which take around 20 minutes and some in less than 10 minutes, the increased scan time and more complex protocol have shown to be one of the major practical factors that hinder the clinical use of dynamic analysis with whole-body imaging.

The study of early dynamics, such as first pass studies (22,23), on the other hand, could enable much shorter scan protocols and enable the estimation of  $k_l$ , which represents the rate of FDG transport from the arterial plasma to the intracellular space with FDG studies. In some literature studies, FDG  $k_l$  was found to be an indicator for identifying

tumor subgroups (24), gene expressions (25), evaluation of chemotherapy response (26), and could be used for the assessment of tumor blood flow (22). FDG  $k_l$  was found to be a valuable parameter for applications other than oncology. In the work by Sarkar, et al (27), the authors found that the  $k_l$  value is helpful for quantifying liver inflammation in nonalcoholic fatty liver disease.

With the recently developed total-body PET system, a dramatic improvement of sensitivity has made it possible to acquire PET images with reasonable image quality in scan times of 60 seconds or less (28,29). With this increase in sensitivity, parametric imaging with high temporal resolution becomes feasible, which in turn may allow accurate parametric imaging using only the early phases of the tracer dynamics. We have developed a method to acquire whole-body parametric images using data acquired from the total-body PET system with a temporal resolution of 1-2 seconds. With the much improved temporal resolution, the delay time of the input function has been shown to be an important factor in VOI-based analysis (30). In this paper, the delay time is included as a voxel-specific parameter that is jointly estimated.

## MATERIALS AND METHODS

### Parametric image reconstruction

For FDG, a 2-tissue compartment model with four rate constants ( $k_1$ ,  $k_2$ ,  $k_3$ , and  $k_4$ ) is often used to model its tracer dynamics. In the 2-tissue compartment model,  $k_1$  and  $k_2$  describe the forward and backward transport of FDG from plasma to tissue.  $k_3$  and  $k_4$  model the phosphorylation and de-phosphorylation process. The accuracy of the measured kinetic parameters in dynamic analysis can be estimated by calculating the sensitivity of the model with respect to each kinetic parameter (31). Zuo et al (32) suggested that  $k_3$  and  $k_4$  cannot be accurately estimated using only the first few minutes of a scan due to low identifiability of these parameters at early times. Therefore, a one-tissue compartment model is used in this paper. The time-activity-curve (TAC) for a specific voxel can be expressed as:

$$C(t) = v_b C_b(t) + (1 - v_b) \left( k_1 \exp(-k_2 t) \otimes C_p(t) \right)$$

Equation 1

where  $v_b$  is the blood fraction in the tissue,  $C_b(t)$  is the TAC for the whole blood,  $C_p(t)$  is the plasma input function,  $C(t)$  is the concentration of FDG in the tissue.  $\otimes$  represents the convolution operation. In the above equation, the whole blood TAC is used for the blood fraction as the intravascular activity includes that from both plasma and blood cells.

With higher temporal resolution and whole-body coverage, the delay time for different regions becomes an important factor. With the inclusion of time-delay, the measured TAC is:

$$C(t) = v_b C_b(t - t_d) + \kappa_1 \exp(-k_2 t) \otimes C_p(t - t_d)$$

Equation 2

where  $t_d$  is the voxel-dependent delay time. For easier computation, the parameter  $\kappa_1 = (1 - v_b)k_1$  is used and estimated instead of  $k_1$ .

Due to the very high temporal resolution used in this study, the TAC for an individual voxel is still expected to be noisy despite the much-increased sensitivity of the scanner. Therefore, it may be beneficial to develop a maximum-likelihood estimation approach that specifically models the noise of the reconstructed dynamic image. Studies in the literature indicate that the voxel values in the image approximately follow a scaled Poisson distribution (33). With this assumption, the log-likelihood function can be derived as:

$$L(\kappa_1, k_2, v_b, t_d) = \sum_t -C(t) + x_t \log(C(t)) - \log(x_t!)$$

Equation 3

where  $x_t$  are the reconstructed dynamic images and is treated as a known measurement in this case. The update equation for  $\kappa_1$ ,  $k_2$ , and  $v_b$  can be derived by maximizing the likelihood in the above equation (see Supplemental Equation 1-5 for derivations):

$$\begin{cases} v_b^{p+1} = \frac{v_b^p}{\sum_t C_b(t - t_d)} \sum_t \frac{C_b(t - t_d) \mathbf{C}(t)}{\widehat{\mathbf{C}}^p(t)} \\ \kappa_1^{p+1} = \frac{\kappa_1^p}{\sum_t e^{-k_2^p t} \otimes C_p(t - t_d)} \sum_t \frac{e^{-k_2^p t} \otimes C_p(t - t_d) \mathbf{C}(t)}{\widehat{\mathbf{C}}^p(t)} \\ k_2^{p+1} = k_2^p \frac{\sum_t t \kappa_1^p (\exp(-k_2^p t)) \otimes C_p(t - t_d)}{\sum_t \frac{t \kappa_1^p (\exp(-k_2^p t)) \otimes C_p(t - t_d) \mathbf{C}(t)}{\widehat{\mathbf{C}}^p(t)}} \end{cases}$$

Equation 4

where  $p$  is the iteration number, and  $\widehat{\mathbf{C}}^p(t) = v_b^p C_b(t - t_d) + \kappa_1^p e^{-k_2^p t} \otimes C_p(t - t_d)$  are the estimated dynamic images.  $\widehat{\mathbf{C}}^p$  is the matrix version of  $\widehat{\mathbf{C}}^p$ , the same is true for other symbols as well. The multiplicative update equations imply positive constraint for  $\kappa_1$ ,  $k_2$ , and  $v_b$ , which is reasonable based on the model. The multiplicative factors for  $\kappa_1$  and  $v_b$  are similar to that from a conventional ML-EM image reconstruction approach, as is the reciprocal of  $k_2$ 's update factor. This similarity makes the implementation straightforward.

A maximum-likelihood gradient-descent approach is used for the estimation of  $t_d$  (see Supplemental Equation 6 for derivations):

$$t_d^{p+1} = t_d^p + s \frac{\partial L(\kappa_1, k_2, v_b, t_d)}{\partial t_d}$$

Equation 5

where  $\frac{\partial L(\kappa_1, k_2, v_b, t_d)}{\partial t_d} = \sum_t (v_b C_b'(t - t_d) - \kappa_1 \exp(-k_2 t) \otimes C_p'(t - t_d)) \left( \frac{x_t}{\widehat{\mathbf{C}}^p(t)} - 1 \right)$ , and  $s$  is the step size of the update. Since the range of time delays are expected to be  $< 1$  minute based on known circulation times, to ensure

convergence, the absolute update for the time delay was set to a fixed value for all voxels in this paper, i.e.  $s = \Delta t / \left| \frac{\partial L(\kappa_1, k_2, v_b, t_d)}{\partial t_d} \right|$ . The value of the update value  $\Delta t$  was set to be 2 seconds in the first few iterations and reduced to 0.2 seconds in later iterations.

In this study, the dynamic images were first reconstructed using 3 iterations with 20 subsets using time-of-flight information. The reconstruction voxel size was 4 mm x 4 mm x 2.89 mm, and attenuation, scatter, randoms, normalization corrections and point spread function modeling were also included during image reconstruction. A 3D Gaussian filter with full width at half maximum of 6 mm was used for noise suppression in the reconstructed dynamic image. An alternate update approach is used to estimate the four parameters. A total of 18 main iterations were used. Within each iteration,  $\kappa_1$  and  $v_b$  were first updated with fixed  $k_2$  and  $t_d$  with nine sub-iterations,  $k_2$  was updated with fixed  $\kappa_1$ ,  $v_b$  and  $t_d$  with 1 sub-iteration, followed by the update of  $t_d$  with fixed  $\kappa_1$ ,  $v_b$  and  $k_2$  using 3 sub-iterations. The same Gaussian smoothing filter was used after every 6 main iterations for the time-delay image and  $\kappa_1$  for better control of noise. With the acquired  $\kappa_1$  and  $v_b$  image, the  $k_l$  image was also generated and compared with  $\kappa_1$ .

To study the accuracy of the estimated parameters, the estimated parameters were compared with volume of interest (VOI)-based analysis. A total of 9 regions were selected (gray matter, white matter, lung, liver, kidney cortex, myocardium, spleen, arm, and thighs, see Fig. 1). A two-tissue irreversible model (2Ti) was also applied on 1-hour long data to compare the estimated  $k_l$  values. In the 2Ti model, the same delay time estimated using the 1-tissue model (1T) was used as the extended time is less likely to contain information regarding the time delay.

### **Patient data and scan protocol**

Two healthy volunteers with an injected activity of  $\sim 220$  MBq were scanned using the uEXPLORER PET scanner with approval of the Ethics Committee of Zhongshan Hospital and after giving informed consent. One volunteer was injected in the leg while the other was injected in the arm. The image data obtained during the first 90 seconds post-injection were used in this study for 1-tissue compartment model analysis.

To obtain an image-derived input function, VOIs over the ascending aorta and the left ventricle (Supplemental Fig. 1) were manually drawn on the PET/CT image and the TACs were acquired. It has been suggested that the best location

for image derived input function is the ascending aorta (34), as it is less affected by respiratory and cardiac motion. The left ventricle is another widely used location due to the relatively large blood pool size (18). The diameter of the ascending aorta VOI was 16 mm and height was 40mm. The boundaries in the left ventricle were excluded in the left ventricle VOI to reduce the effect of respiratory motion, and the total volume was about the same as the ascending aorta VOI. Whole blood-plasma correction was applied on the TAC  $C_b(t)$  to estimate the plasma input function  $C_p(t)$ . The correction equations and values are based on the method and parameters published in the literature (equation 2 in (35), where the hematocrit is 0.42 and the equilibration time constant is  $0.23 \text{ min}^{-1}$ ).

## RESULTS

Fig 2 shows the first 90 seconds of the image-derived plasma input function for volunteer 1 using the reconstructed dynamic images acquired using ascending aorta VOI and left ventricle VOI. Image voxel values were directly used without calibration of activity concentrations using a well counter. The calibration scale factor cancels out in the analysis and therefore is not needed. The TACs were almost identical except the 1 second delay time. With the added delay time modeling, the results are expected to be the same with the use of left ventricle as the input function. The TAC from the ascending aorta was used for the input function.

Fig. 3 shows the acquired maximum intensity projection from the reconstructed  $\kappa_1$  and  $v_b$  images. The reconstructed parametric images  $v_b$ ,  $\kappa_1$ ,  $k_2$ , and  $t_d$  from volunteer 1 are shown in Fig. 4. The  $k_l$  image was also calculated using  $v_b$  and  $\kappa_1$ . The SUV image acquired from the same time periods (0-90s) is also shown for comparison.  $v_b$  represents the plasma volume fraction in the tissue, which is clearly visible in the blood pool of the heart and the in aorta. The visual difference between  $k_l$  and  $\kappa_1$  is in general small except for the myocardium region. High  $k_l$  values are observed in the spleen and kidneys. Moderate  $k_l$  values are observed in the liver and myocardium. High  $k_l$  was also observed in some blood vessels (mostly veins), likely the result of dispersion of the plasma input function in these vessels. The abnormal signal in the veins near the injection site suggested possible retrograde pooling in the veins. Very large  $k_2$  values are also observed in some blood vessels for the same reason. Large delay times were observed in the liver (>10 seconds) and extremities (~30 seconds) when compared with the delay time in the lungs. The large delay time in the liver region

is likely caused by the dual blood supply from both the hepatic artery and the portal vein (36), and the algorithm approximated the portal vein input function with the arterial input function by means of a time delay. The time-delay image was also able to be used for the illustration of the circulatory system. In volunteer 1, FDG was first injected into a vein located on the leg and then traveled to the right ventricle of the heart. From there the tracer was moves into the lungs and back to the left ventricle of the heart, where the tracer was pumped via the arterial system to other organs. The measured delay times (relative to the ascending aorta),  $k_1$ , and  $v_b$  for different organs is given in Table 1.

Using VOI analysis, the estimated  $k_1$ ,  $k_2$ , and blood fraction  $v_b$  using the 1T model with 90 seconds of data was compared with the same parameters calculated using the 2Ti model with 1-hour long data. Fig. 5 shows the relationships of the estimated values. It can be observed that for  $k_1$  and  $v_b$ , both approaches yield similar results (coefficient of determination of linear fitting for  $k_1$  is 0.97, for blood fraction is 0.95). Some large differences were observed in  $k_2$ , suggesting that  $k_2$  can't be accurately estimated from the 90 seconds data. The estimated  $k_1$  using VOI-based analysis was also compared with the  $k_1$  acquired from the parametric image and is given in Table 1. For most VOIs, the differences of  $k_1$  are small. Underestimation of  $k_1$  was observed in myocardium and kidney cortex VOIs, which is likely due to the application of the Gaussian filter, which introduced additional partial volume effects and affected the quantitative values within these relatively small structures.

Fig. 6 shows the TACs for myocardium, brain, liver, and lung. The average parameters within the VOI were used to estimate the fitted curves. Due to the use of the ascending aorta as the input function, a positive delay time was observed in the liver and negative delay time in the myocardium and lung, with minimal delay time observed in the brain. The difference between the curves from averaged voxel-based parameters and from the VOI-based parameters was relatively small, indicating a small bias from the voxel-based analysis. Even though in general, the model used in this paper was able to predict the TAC from different organs, with the use of high temporal resolution, discrepancies can be observed in some organs such as the liver.

## DISCUSSION

The preliminary study shows that the  $k_1$  estimated using 90-second data in general agrees with that derived from a much longer scan (1 hour). The same agreement was not found for  $k_2$ , indicating that the estimated  $k_2$  is less accurate in shorter scans. High  $k_1$  values were detected in some venous blood pools, such as the jugular veins, venous sinuses, and portal veins, while high blood fractions were observed in arterial blood pools such as the carotid arteries (Fig. 3). The high  $k_1$  values in some blood pools regions are likely caused by the dispersion effects modeled by the one tissue compartment model (37). This information may be used for providing further physiological insights and better kinetic modeling. For instance, the  $k_1$  in the venous blood pools of the brain may represent the combined effects of the glucose passing through the brain's vasculature structure, and the small extraction of tracers within the brain. The  $k_1$  in the portal veins may also be used to develop a more accurate model for the liver. The modeling of the delay times in the kinetic model not only enabled better model fitting but also produced time-delay image which could be used for providing additional information, for example as a biomarker for assessing blood delivery and vessel occlusion.

However, our method did not model the dispersion effects of the input function for different organs. Another limitation of the proposed approach is the use of a single model for the whole body. For instance, the dual blood supplies (portal veins and arteries) in the liver region (32) were not modeled. The use of a single input function resulted in some quantitative inaccuracy and further studies are required for more accurate parametric imaging. The image-based input function in this study was also not validated using arterial blood samples, but the feasibility has already been proven in the literature (18). Due to the very concentrated and rapidly changing tracer distribution in the first few seconds following injection, scatter corrections may not be accurate enough. One possible example of this is the low delay times in the regions near the injection site in the time-delay image. Another example is the small increase in the liver TAC around 20 seconds after injection, which we believe was caused by the inaccurate scatter correction from the very high activity level during the injection.

Two different injection sites were used in our study. Initially the leg was chosen as this enabled the injection site to be closer to the end of the gantry, thus requiring a shorter tube connecting the syringe and the needle; however, a major challenge for injection in the leg is the difficulty for the technologist to find the appropriate vein. Subsequent to the

first patient, we have chosen to perform all injections in the antecubital fossa, which follows conventional practice and has not led to significant difficulties (38).

While our method was developed using FDG, the same methodology can be applied to other tracers as well. More benefit can be expected for radionuclides with much shorter half-life such as  $^{15}\text{O}$  or  $^{82}\text{Rb}$ . The acquired FDG  $k_1$  image can also be used to examine the relationship between blood flow and metabolism, which may help diagnosis in some pathophysiology such as hyperemic states of areas of brain tissue post stroke. For FDG scans, a practical implementation of the proposed approach can still be challenging, as traditionally FDG imaging mostly focuses on the later period when equilibrium is reached. The combination with a later time scans may be the solution; however, future studies are required to address the clinical or technical challenges for that protocol.

Future studies using patient data are required for a better understanding of the full potential of the clinical significance of the proposed method.

## CONCLUSIONS

In this study, we demonstrated that with the use of a ultra-high sensitivity total-body PET scanner, it is possible to achieve whole-body parametric image reconstruction using only the early stage of the scan (within the first two minutes post-injection), making it much easier to incorporate into the daily clinical route. However, only fast parameters such as  $k_1$  can be estimated using this ultra-short scan duration. We have also shown that with the much-improved temporal resolution due to improved sensitivity, organ-dependent delay time becomes an important factor to consider in the analysis of whole-body early-stage dynamics.

## DISCLOSURES

Tao Feng and Hongdi Li are employed by UIH America, Inc, Yizhang Zhao is employed by United Imaging Healthcare. Simon R. Cherry and Ramsey D. Badawi have a research agreement with United Imaging Healthcare. UC Davis has a revenue-sharing agreement with United Imaging Healthcare. No other potential conflicts of interest relevant to this article exist.

**KEY POINTS**

QUESTION: Can whole-body first-pass parametric imaging be achieved using an ultra-short scanning protocol?

PERTINENT FINDINGS: We have demonstrated the possibility to generate whole-body parametric images such as  $k_1$  (a possible indicator for tumor identification), blood fraction, and time-delay images that illustrate the circulatory system, from dynamic scans as short as 90 seconds using the uEXPLORER scanner.

IMPLICATIONS FOR PATIENT CARE: Produces added value (a potential biomarker for tumor identification and other disease identification) with minimal added scanner time.

**REFERENCES**

1. Lindholm P, Minn H, Leskinen-Kallio S, Bergman J, Ruotsalainen U, Joensuu H. Influence of the blood glucose concentration on FDG uptake in cancer—a PET study. *J Nucl Med.* 1993;34:1-6.
2. Adams MC, Turkington TG, Wilson JM, Wong TZ. A systematic review of the factors affecting accuracy of SUV measurements. *Am J Roentgenol.* 2010;195:310-320.
3. Boellaard R. Need for standardization of 18F-FDG PET/CT for treatment response assessments. *J Nucl Med.* 2011;52:93S-100S.
4. Hamberg LM, Hunter GJ, Alpert NM, Choi NC, Babich JW, Fischman AJ. The dose uptake ratio as an index of glucose metabolism: useful parameter or oversimplification? *J Nucl Med.* 1994;35:1308.
5. Nesterov S V, Deshayes E, Sciagrà R, et al. Quantification of myocardial blood flow in absolute terms using 82Rb PET imaging: the RUBY-10 study. *JACC Cardiovasc Imaging.* 2014;7:1119-1127.
6. Muzi M, Vesselle H, Grierson JR, et al. Kinetic analysis of 3'-deoxy-3'-fluorothymidine PET studies: validation studies in patients with lung cancer. *J Nucl Med.* 2005;46:274-282.
7. Gulaldi N, Xia J, Feng T, et al. Modeling of the renal kinetics of the AT1 receptor specific PET radioligand [11C] KR31173. *Biomed Res Int.* 2013;2013:1-12.
8. Kamasak ME, Bouman CA, Morris ED, Sauer K. Direct reconstruction of kinetic parameter images from dynamic PET data. *IEEE Trans Med Imaging.* 2005;24:636-650.
9. Zhang X, Xie Z, Berg E, et al. Total-body dynamic reconstruction and parametric imaging on the uEXPLORER. *J Nucl Med.* 2019;jnumed-119.

10. Logan J. Graphical analysis of PET data applied to reversible and irreversible tracers. *Nucl Med Biol.* 2000;27:661-670.
11. Patlak CS, Blasberg RG. Graphical evaluation of blood-to-brain transfer constants from multiple-time uptake data. Generalizations. *J Cereb Blood Flow Metab.* 1985;5:584-590.
12. Wu H, Dimitrakopoulou-Strauss A, Heichel TO, et al. Quantitative evaluation of skeletal tumours with dynamic FDG PET: SUV in comparison to Patlak analysis. *Eur J Nucl Med.* 2001;28:704-710.
13. Visser EP, Philippens MEP, Kienhorst L, et al. Comparison of tumor volumes derived from glucose metabolic rate maps and SUV maps in dynamic 18F-FDG PET. *J Nucl Med.* 2008;49:892-898.
14. Cunningham VJ, Jones T. Spectral analysis of dynamic PET studies. *J Cereb Blood Flow Metab.* 1993;13:15-23.
15. Watabe H, Jino H, Kawachi N, et al. Parametric imaging of myocardial blood flow with 15O-water and PET using the basis function method. *J Nucl Med.* 2005;46:1219-1224.
16. Karakatsanis NA, Lodge MA, Tahari AK, Zhou Y, Wahl RL, Rahmim A. Dynamic whole-body PET parametric imaging: I. Concept, acquisition protocol optimization and clinical application. *Phys Med Biol.* 2013;58:7391.
17. Rahmim A, Lodge MA, Karakatsanis NA, et al. Dynamic whole-body PET imaging: principles, potentials and applications. *Eur J Nucl Med Mol Imaging.* 2018:1-18.
18. de Geus-Oei L-F, Visser EP, Krabbe PFM, et al. Comparison of image-derived and arterial input functions for estimating the rate of glucose metabolism in therapy-monitoring 18F-FDG PET studies. *J Nucl Med.* 2006;47:945-949.
19. Feng T, Tsui BMW, Li X, et al. Image-derived and arterial blood sampled input functions for quantitative PET

imaging of the angiotensin II subtype 1 receptor in the kidney. *Med Phys*. 2015;42:6736-6744.

20. Takikawa S, Dhawan V, Spetsieris P, et al. Noninvasive quantitative fluorodeoxyglucose PET studies with an estimated input function derived from a population-based arterial blood curve. *Radiology*. 1993;188:131-136.
21. Rissanen E, Tuisku J, Luoto P, et al. Automated reference region extraction and population-based input function for brain [11C] TMSX PET image analyses. *J Cereb Blood Flow Metab*. 2015;35:157-165.
22. Mullani NA, Herbst RS, O'Neil RG, Gould KL, Barron BJ, Abbruzzese JL. Tumor blood flow measured by PET dynamic imaging of first-pass 18F-FDG uptake: a comparison with 15O-labeled water-measured blood flow. *J Nucl Med*. 2008;49:517-523.
23. Cochet A, Pigeonnat S, Khoury B, et al. Evaluation of breast tumor blood flow with dynamic first-pass 18F-FDG PET/CT: comparison with angiogenesis markers and prognostic factors. *J Nucl Med*. 2012;53:512.
24. Sugawara Y, Zasadny KR, Grossman HB, Francis IR, Clarke MF, Wahl RL. Germ cell tumor: differentiation of viable tumor, mature teratoma, and necrotic tissue with FDG PET and kinetic modeling. *Radiology*. 1999;211:249-256.
25. Cheng C, Klippel S, Koczan D, Willis S, Pan L, Sachpekidis C. Gene Expression Profiling of Colorectal Cancer by Correlation with 18F-FDG Kinetics as Measured by Dynamic Positron Emission Tomography-Computed Tomography (dPET-CT): Dependency on Cadherin-Related Genes and Hypoxia. *Clin Oncol*. 2017;2:1179.
26. Song S, Deng C, Wen L, et al. 18F-FDG PET/CT-related metabolic parameters and their value in early prediction of chemotherapy response in a VX2 tumor model. *Nucl Med Biol*. 2010;37:327-333.
27. Sarkar S, Corwin MT, Olson KA, et al. Pilot study to diagnose nonalcoholic steatohepatitis with dynamic 18F-FDG PET. *Am J Roentgenol*. 2019;212:529-537.

28. Cherry SR, Badawi RD, Karp JS, Moses WW, Price P, Jones T. Total-body imaging: transforming the role of positron emission tomography. *Sci Transl Med*. 2017;9:eaaf6169.
29. Badawi RD, Shi H, Hu P, et al. First human imaging studies with the EXPLORER total-body PET scanner. *J Nucl Med*. 2019;60:299-303.
30. Lammertsma AA, Cunningham VJ, Deiber MP, et al. Combination of dynamic and integral methods for generating reproducible functional CBF images. *J Cereb Blood Flow Metab*. 1990;10:675-686.
31. Mankoff DA, Muzi M, Zaidiy H. Quantitative analysis in nuclear oncologic imaging. In: Quantitative Analysis in Nuclear Medicine Imaging. Springer; 2006:494-536.
32. Zuo Y, Sarkar S, Corwin MT, Olson KA, Badawi RD, Wang G. Structural and practical identifiability of dual-input kinetic modeling in dynamic PET of liver inflammation. *Phys Med Biol*. 2019.
33. Wilson DW, Tsui BMW, Barrett HH. Noise properties of the EM algorithm. II. Monte Carlo simulations. *Phys Med Biol*. 1994;39:847.
34. Van Der Weerd AP, Klein LJ, Boellaard R, Visser CA, Visser FC, Lammertsma AA. Image-derived input functions for determination of MRGlu in cardiac 18F-FDG PET scans. *J Nucl Med*. 2001;42:1622-1629.
35. Wahl LM, Asselin M-C, Nahmias C. Regions of interest in the venous sinuses as input functions for quantitative PET. *J Nucl Med*. 1999;40:1666-1675.
36. Munk OL, Bass L, Roelsgaard K, Bender D, Hansen SB, Keiding S. Liver kinetics of glucose analogs measured in pigs by PET: importance of dual-input blood sampling. *J Nucl Med*. 2001;42:795-801.
37. Iida H, Kanno I, Miura S, Murakami M, Takahashi K, Uemura K. Error analysis of a quantitative cerebral blood flow measurement using H215O autoradiography and positron emission tomography, with respect to the

dispersion of the input function. *J Cereb Blood Flow Metab.* 1986;6:536-545.

38. McBride K and Hunt HL. Bolus injection technique for uEXPLORER 18F-FDG PET/CT dynamic scans. *Journal of Nuclear Medicine* 61.supplement 1 (2020): 3084-3084.

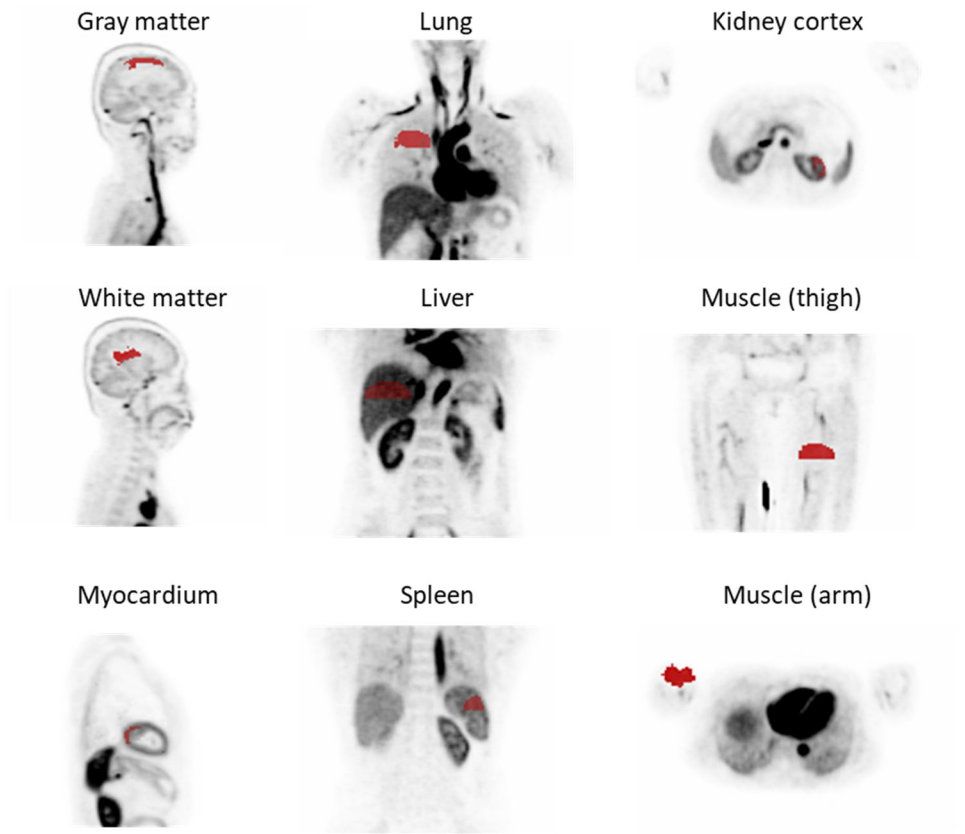


Fig. 1 The volumes of interests used for the parameter estimation

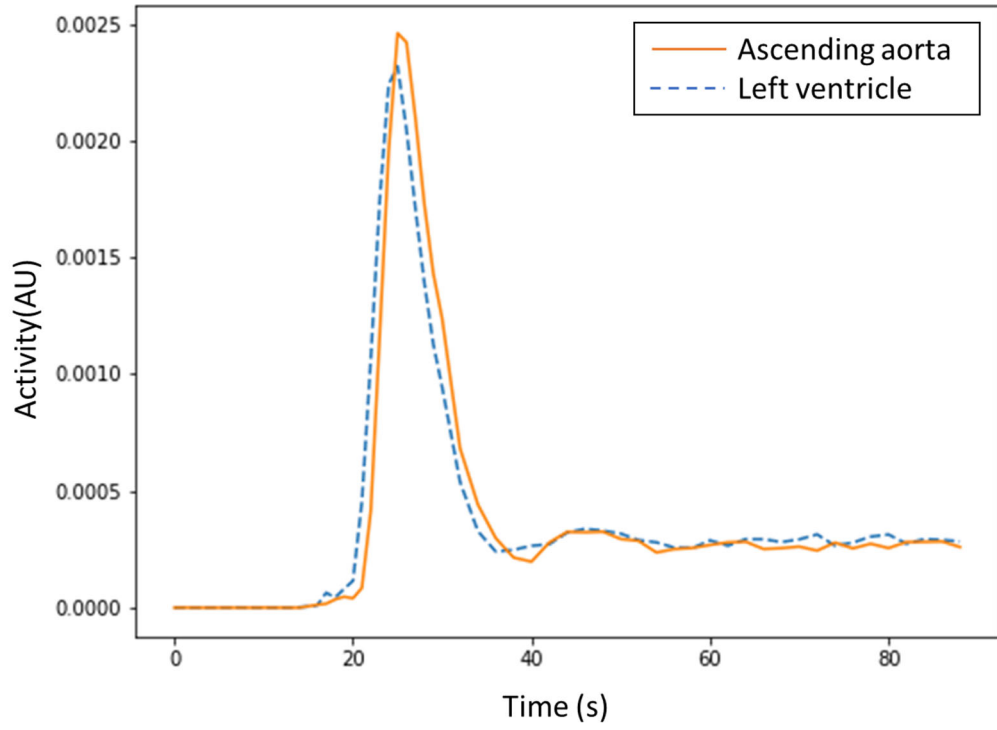


Fig. 2 Image-derived input function for the first 90 seconds post-injection.

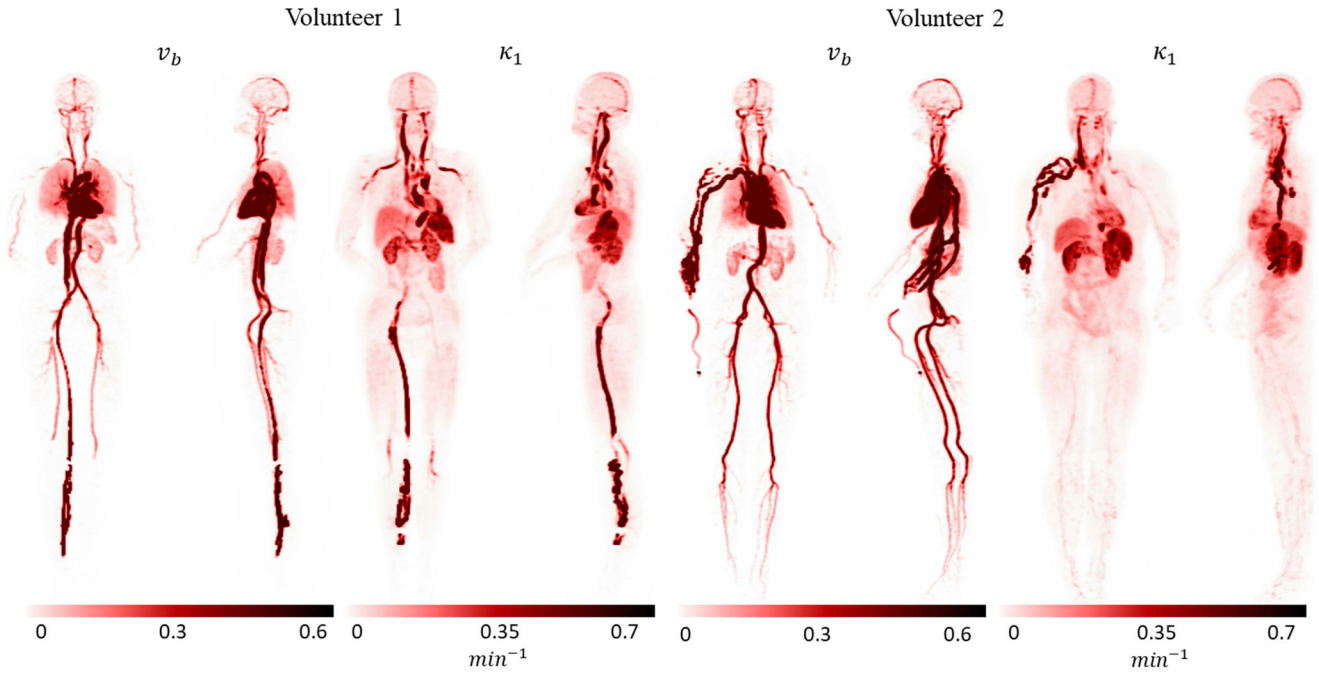


Fig. 3 Maximum intensity projection image of the reconstructed parametric images  $v_b$  and  $\kappa_1$  acquired using the proposed approach.

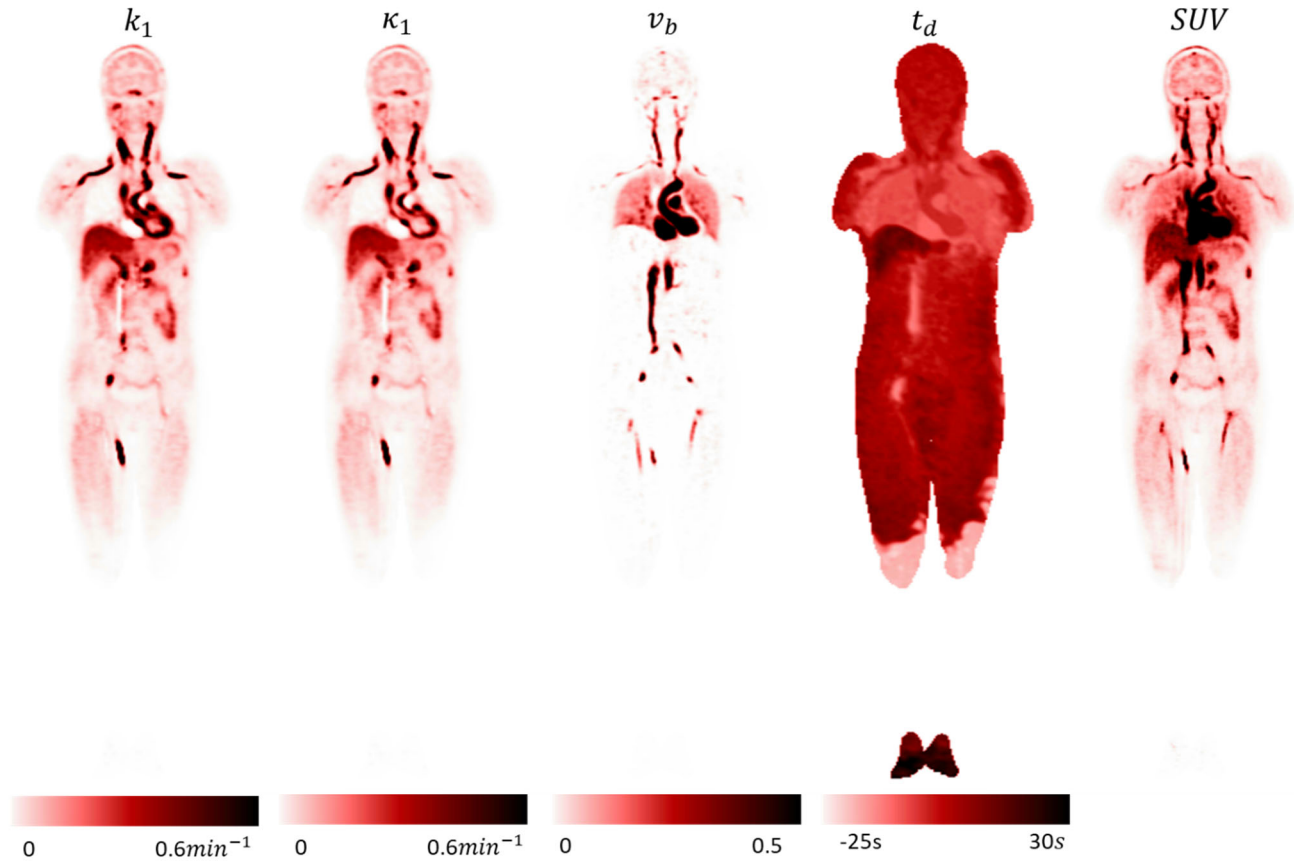


Fig. 4. A coronal plane of the reconstructed  $k_l$ ,  $\kappa_1$ ,  $v_b$ , and  $t_d$  parametric images using the proposed method from volunteer 1, together with the SUV image

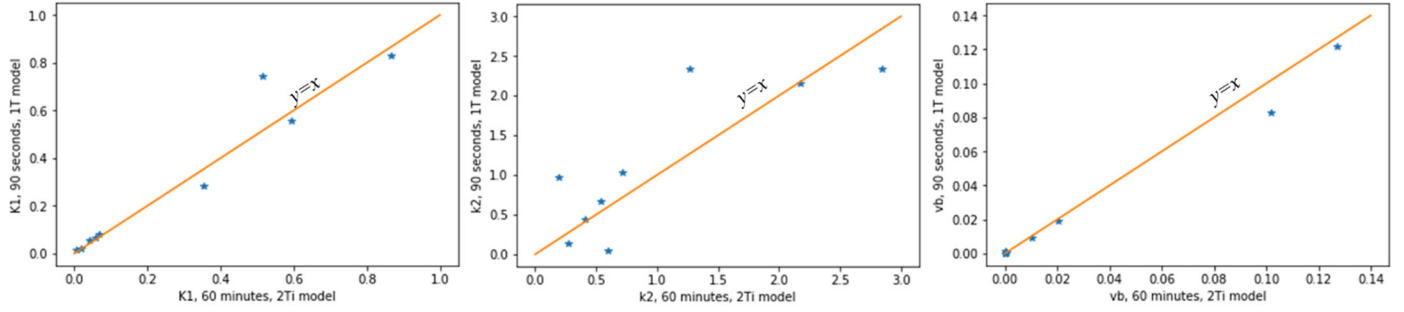


Fig. 5. The estimated  $k_1$ ,  $k_2$ , and  $v_b$  for 9 VOIs using 1-tissue model with 90 seconds data (y-axis) and 2-tissue irreversible model with 1 hour data (x-axis).

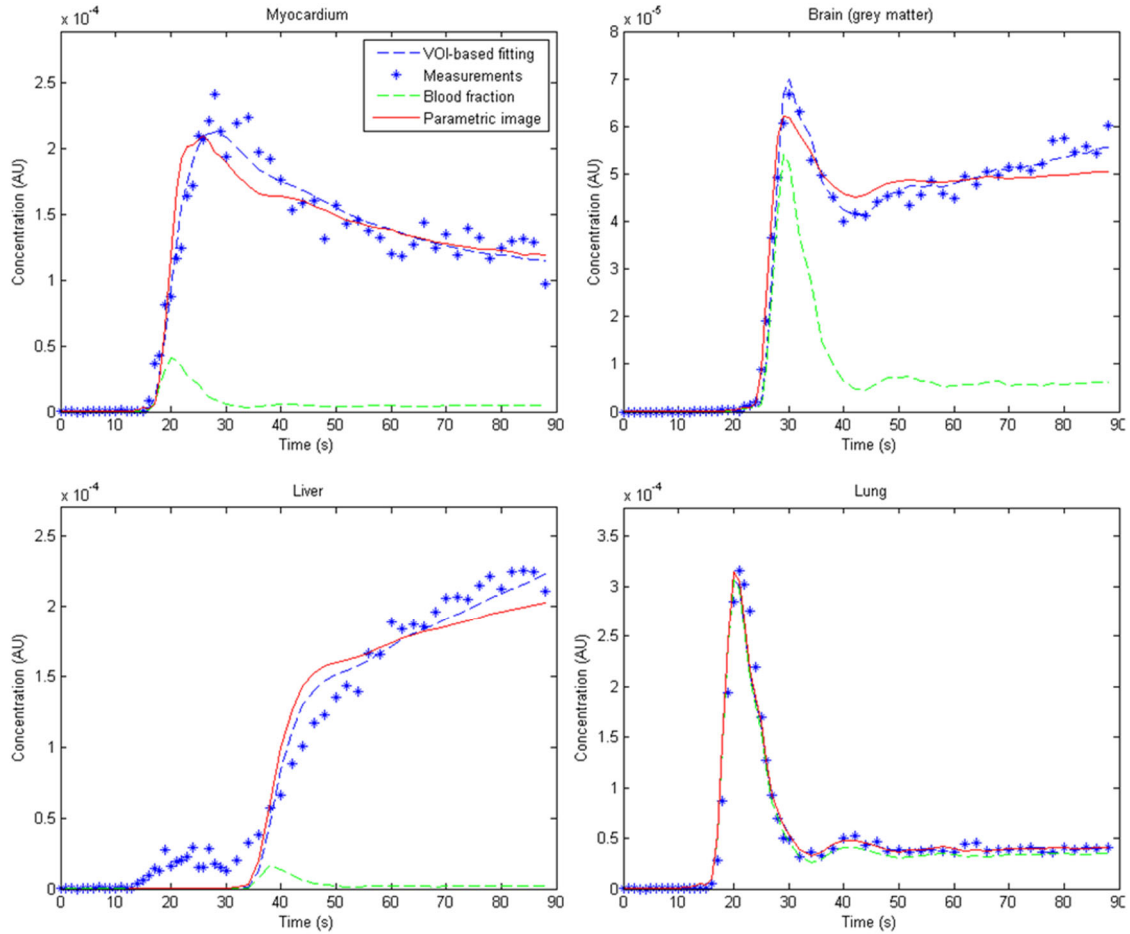


Fig. 6 The time-activity-curve (TAC) measured from the dynamic frames (blue dots) and the fitted curves using the proposed method, and a fitting based on the TAC from the VOI in four different organs: myocardium, brain, liver, and lung. For better illustration of the delay time, the corresponding blood fraction in the TAC was also plotted.

Table 1. Estimated  $k_I$  and delay time (relative to ascending aorta) in different organs

Organs	Gray matter	White matter	Myocardium	Liver	Kidney cortex	Spleen	Lung	Arm	Thigh
$k_I$ ( $\text{min}^{-1}$ ) VOI analysis	0.08	0.05	0.56	0.39	0.75	0.92	0.02	0.02	0.06
$k_I$ ( $\text{min}^{-1}$ ) Parametric image	$0.09 \pm 0.02$	$0.06 \pm 0.01$	$0.45 \pm 0.10$	$0.33 \pm 0.04$	$0.54 \pm 0.08$	$0.73 \pm 0.13$	$0.02 \pm 0.02$	$0.02 \pm 0.01$	$0.06 \pm 0.03$
$C_b$ VOI analysis	0.020	0.01	0.02	0.006	0.08	0.006	0.12	0.0004	0.0
$C_b$ Parametric image	$0.020 \pm 0.01$	$0.007 \pm 0.005$	$0.05 \pm 0.04$	$0.003 \pm 0.005$	$0.11 \pm 0.03$	$0.03 \pm 0.02$	$0.12 \pm 0.03$	$0.0009 \pm 0.001$	$0.004 \pm 0.01$
Time delay (s)	3.9	3.7	-1.2	13.1	4.7	3.1	-3.8	10.8	8.6

Supplement 1: Maximum likelihood estimation method:

For a fixed voxel, the kinetic model is

$$C_t(\lambda) = v_b C_b(t - t_d) + \kappa_1 \exp(-k_2 t) \otimes C_p(t - t_d)$$

Supplemental Equation 1

where  $\lambda$  represents the four parameters  $v_b, \kappa_1, k_2$ , and  $t_d$ .

Assuming the voxel value of the reconstructed dynamic image  $x_t$  is Poisson distributed, the loglikelihood is:

$$L(\lambda) = \sum_t -C_t(\lambda) + x_t \log(C_t(\lambda)) - \log(x_t!)$$

Supplemental Equation 2

The derivative for the parameter  $\lambda$  is

$$\frac{\partial L(\lambda)}{\partial \lambda} = \sum_t \frac{\partial L(\lambda)}{\partial C_t} \frac{\partial C_t}{\partial \lambda} = \sum_t \frac{\partial C_t}{\partial \lambda} \left( \frac{x_t}{C_t(\lambda)} - 1 \right)$$

Supplemental Equation 3

1 Update equation for  $\kappa_1$  and  $v_b$

For  $\kappa_1$  and  $v_b$ , the condition  $\frac{\partial C_t}{\partial \lambda} > 0$  is always true, and the conventional ML-EM approach can be directly applied in this case. The update equation for  $\lambda$  at voxel  $j$  is:

$$\lambda_j^{n+1} = \frac{\lambda_j^n}{\sum_t \frac{\partial C_{j,t}}{\partial \lambda_j}} \sum_t \frac{\partial C_{j,t}}{\partial \lambda_j} x_{j,t} C_{j,t}(\lambda_j^n)$$

## Supplemental Equation 4

Supplemental Equation 4 is used to derive the update formula for  $\kappa_1$  and  $v_b$ . The above equation is very similar to the conventional ML-EM update for image reconstruction.

2 Update equation for  $k_2$ 

For  $k_2$ , the condition  $\frac{\partial C_t}{\partial \lambda} < 0$  is always true, and the model requires  $k_2$  to be positive. While Equation A.5 can be directly applied, it can be seen that with an improper choice of  $s$ ,  $k_2$  estimated using the above equation could be negative, which is undesirable. An easy approach for enforcing the positive constraint for  $k_2$  and to determine the best step size is to convert the additive update equation to a multiplicative update.

Let  $s = \frac{\lambda_j^n}{-\sum_i \frac{\partial C_{j,t}}{\partial \lambda_j} * \frac{x_{j,t}}{c_{j,t}(\lambda_j^n)}}$ , it can be seen that as long as  $\lambda_j^n > 0$ ,  $\frac{\partial C_{j,t}}{\partial \lambda_j} < 0$ ,  $s > 0$  is true. The update equation becomes:

$$\lambda_j^{n+1} = \lambda_j^n + \frac{\lambda_j^n}{-\sum_i \frac{\partial C_{j,t}}{\partial \lambda_j} * \frac{x_{j,t}}{c_{j,t}(\lambda_j^n)}} \sum_t \frac{\partial C_{j,t}}{\partial \lambda_j} \left( \frac{x_{j,t}}{c_{j,t}(\lambda_j^n)} - 1 \right) = \frac{\lambda_j^n \sum_t \frac{\partial C_{j,t}}{\partial \lambda_j}}{\sum_i \frac{\partial C_{j,t}}{\partial \lambda_j} * \frac{x_{j,t}}{c_{j,t}(\lambda_j^n)}}$$

## Supplemental Equation 5

The conversion from an additive update formulation to multiplicative update formulation ensures the positive constraint. It can be observed that the multiplicative update factor for the above equation is the reciprocal of a typical ML-EM update approach. The similarity makes its implementation straightforward.

3 Update equation for  $t_d$ 

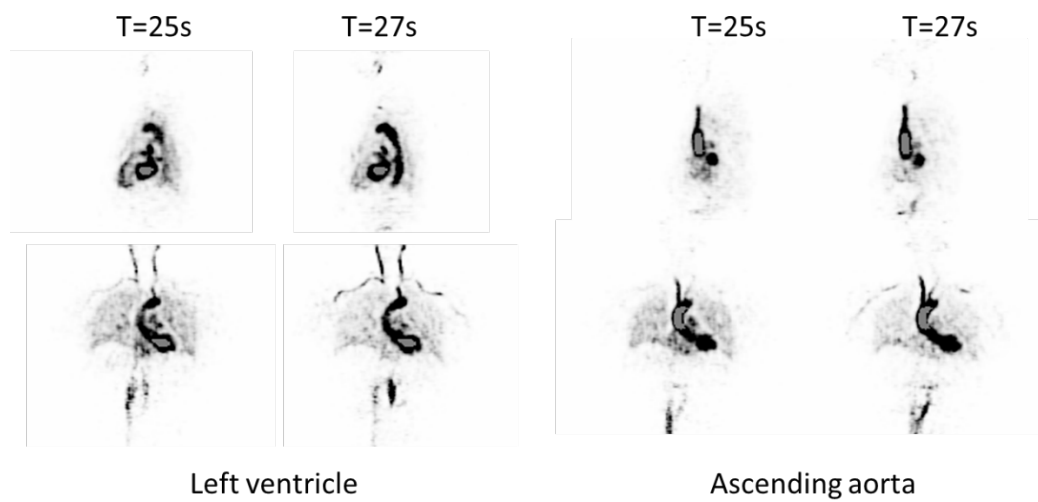
For the parameter  $t_d$ , the condition that  $\frac{\partial C_t}{\partial \lambda} > 0$  no longer holds, and a gradient descent approach can be used for update:

$$\lambda_j^{n+1} = \lambda_j^n + s \frac{\partial L(\lambda)}{\partial \lambda} = \lambda_j^n + s \sum_t \frac{\partial C_{j,t}}{\partial \lambda_j} \left( \frac{x_{j,t}}{c_{j,t}(\lambda_j^n)} - 1 \right)$$

## Supplemental Equation 6

where  $s$  is the step size and  $s > 0$ .

## Supplement 2. Volumes of interests for input functions



Supplemental Fig. 1 The VOIs for ascending aorta-based input function and left ventricle-based input function. Respiratory motion could be observed in the left ventricle region and therefore limiting the size of the VOI. The ascending aorta was less affected by respiratory motion.